

Contents lists available at [SciVerse ScienceDirect](#)

# Medical Image Analysis

journal homepage: [www.elsevier.com/locate/media](http://www.elsevier.com/locate/media)

## Complete valvular heart apparatus model from 4D cardiac CT

Sasa Grbic<sup>a,b,\*</sup>, Razvan Ionasec<sup>a</sup>, Dime Vitanovski<sup>a</sup>, Ingmar Voigt<sup>a</sup>, Yang Wang<sup>a</sup>, Bogdan Georgescu<sup>a</sup>, Nassir Navab<sup>b</sup>, Dorin Comaniciu<sup>a</sup>

<sup>a</sup>Image Analytics and Medical Informatics, Siemens Corporate Research, Princeton, New Jersey, 08540 USA

<sup>b</sup>Computer Aided Medical Procedures, Technical University Munich, Germany

### ARTICLE INFO

#### Article history:

Available online xxxxx

#### Keywords:

Cardiac modeling  
Heart valves modeling  
Multilinear shape models

### ABSTRACT

The cardiac valvular apparatus, composed of the aortic, mitral, pulmonary and tricuspid valves, is an essential part of the anatomical, functional and hemodynamic characteristics of the heart and the cardiovascular system as a whole. Valvular heart diseases often involve multiple dysfunctions and require joint assessment and therapy of the valves. In this paper, we propose a complete and modular patient-specific model of the cardiac valvular apparatus estimated from 4D cardiac CT data. A new constrained Multi-linear Shape Model (cMSM), conditioned by anatomical measurements, is introduced to represent the complex spatio-temporal variation of the heart valves. The cMSM is exploited within a learning-based framework to efficiently estimate the patient-specific valve parameters from cine images. Experiments on 64 4D cardiac CT studies demonstrate the performance and clinical potential of the proposed method. Our method enables automatic quantitative evaluation of the complete valvular apparatus based on non-invasive imaging techniques. In conjunction with existent patient-specific chamber models, the presented valvular model enables personalized computation modeling and realistic simulation of the entire cardiac system.

Crown Copyright © 2012 Published by Elsevier B.V. All rights reserved.

### 1. Introduction

The valves are essential anatomical structures regulating the heart chamber hemodynamics and the blood flow between the heart and the systemic and pulmonary circulations. Valvular Heart Disease (VHD) which affects 2.5% of the global population and requires yearly over 100,000 surgeries in the United States alone, is a representative instance for the growing public health problem provoked by cardiovascular diseases. Heart valve operations are the most expensive and the riskiest cardiac procedures, with an average cost of \$141,120 and 4.9% in-hospital death rate (Donald et al., 2009).

Due to the strong anatomical, functional and hemodynamic inter-dependency of the heart valves, VHDs do not affect only one valve, but rather several valves are impaired. Recent studies demonstrate strong influence of pulmonary artery systolic pressure on the tricuspid regurgitation severity (Mutlak et al., 2009). In Lansac et al. (2002), Timek et al. (2003) the simultaneous evaluation of aortic and mitral valves is encouraged, given the fibrous aortic-mitral continuity, which anchors the left side valves and facilitates the reciprocal opening and closing motion during the cardiac cycle. Moreover, in patients with mitral and tricuspid valve regurgitation,

joint surgery is recommended to minimize the risk for successive heart failure or reduced functional capacity. Complex procedures mostly performed in patients with congenital heart diseases, such as the Ross operation, in which the aortic valve is replaced with the pulmonary, require comprehensive quantitative and qualitative evaluation of the heart valves. Morphological and functional assessment of the complete heart valve apparatus is crucial for clinical decision making during diagnosis and severity assessment as well as treatment selection and planning.

Decisions in valvular disease management increasingly rely on non-invasive imaging. The quality of acquired information, as well as the accessibility and cost effectiveness of each medical imaging modality has radically improved over the past decades. Techniques like cardiac Computed Tomography (CT) enable dynamic four dimensional scanning of the beating heart over the whole cardiac cycle. Such volumetric time-resolved data encode comprehensive structural and dynamic information, which however is barely exploited in current clinical practice, due to its size and complexity as well as the lack of appropriate medical systems in order to utilize the extensive image information.

The progress in medical imaging is matched by important advances in surgical techniques, bioprosthetic valves, robotic surgery and percutaneous interventions, which have led to a twofold increase in the number of valve procedures performed in the United States since 1985 (Jablockow, 2007). According to the Millennium Research Group, percutaneous heart valve therapies will dominate

\* Corresponding author at: Image Analytics and Medical Informatics, Siemens Corporate Research, Princeton, New Jersey, 08540 USA. Tel.: +1 (609) 734 6544.

E-mail address: [sasa.grbic@siemens.com](mailto:sasa.grbic@siemens.com) (S. Grbic).

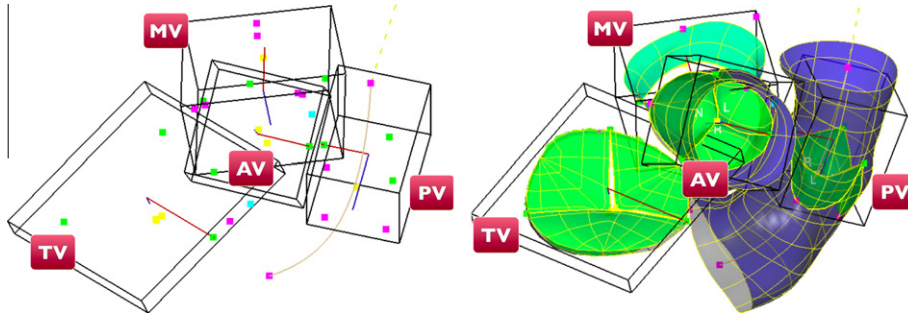


**Fig. 1.** Complete heart valves model consisting of aortic valve (AV), mitral valve (MV), pulmonary valve (PV) and tricuspid valve (TV). Left: Similarity transform illustrated as a bounding box and anatomical landmarks. Right: Complete mesh surface model.

the future and cover up to 41.1% of all valve procedures by 2012. Powerful computer-aided tools for extensive non-invasive assessment, planning and guidance are mandatory to continuously decrease the level of invasiveness and maximize effectiveness of valve therapy.

An increased holistic view of the heart, demanded by clinicians is in perfect accordance with the tremendous scientific effort worldwide, such as the Virtual Physiological Human project (Clapworthy et al., 2008), geared towards multi-scale physiological modeling and simulation, which will promote personalized, preventive and predictive healthcare. However, the majority of cardiac models to date are focused on representation of the left or right ventricle (Fritz et al., 2006), while very few include the left and right atrium (Zheng et al., 2008; Lorenz and von Berg, 2006; Zhuang et al., 2010a; Huang et al., 2007; Zhuang et al., 2010b; Ecabert et al., 2008) but none explicitly handles the valves. Recently introduced models of the aortic valve (Waechter et al., 2010; Ionasec et al., 2008), the mitral valve (Schneider et al., 2010; Conti et al., 2010) and the aortic-mitral coupling (Ionasec et al., 2009; Veronesi et al., 2009; Ionasec et al., 2010) do not incorporate the right side valves. A critical component for a patient-specific computation model of the entire heart and realistic cardiovascular simulations, which was not reported yet in the literature, is a personalized and complete representation of the valvular apparatus Grbic et al. (2010).

In this paper we propose a complete and modular model of the heart valves comprising the anatomy of the aortic, mitral, tricuspid and pulmonary valves (illustrated in Fig. 1) as well as their morphological, functional and pathological variations. The patient-specific valvular apparatus is estimated non-invasively from 4D Computed Tomography images, using a discriminative learning-based approach. The global valve location and motion, as well as the non-rigid movement of anatomical valvular landmarks, are computed within the Marginal Space Learning (MSL) (Zheng et al., 2007) and Trajectory Spectrum Learning (TSL) (Ionasec et al., 2009) frameworks. A novel anatomical constrained Multi-linear Shape Model (cMSM) is introduced to capture complex spatio-temporal statistics, and in conjunction with robust boundary detectors, it is applied to extract the complete valvular anatomy and motion.

## 2. Physiological model of the heart valves

In this section we introduce the complete heart valves model, which includes the aortic, mitral, tricuspid and pulmonary valves, and captures their morphological, functional and pathological variations. To reduce anatomical complexity and facilitate effective estimation, the heart valve model is represented on three abstraction layers: global motion model – which represents the global location and motion of each valve; anatomical landmark model – representing the motion of the corresponding anatomic land-

marks; complete valve model – which parameterizes the full anatomy and dynamics of the valves using dense surface meshes.

### 2.1. Global motion model

The global dynamic variation of each valve is parameterized through a similarity transformation in the Euclidean three-dimensional space, which includes nine parameters.

$$\mathbf{B}_t = \{(c_x, c_y, c_z), (\alpha_x, \alpha_y, \alpha_z), (s_x, s_y, s_z)\} \quad t \in 1 \dots T \quad (1)$$

$(c_x, c_y, c_z)$  is the translation,  $(\alpha_x, \alpha_y, \alpha_z)$  the quaternion representation of the rotation,  $(s_1, s_2, s_3)$  the similarity transform scaling factors and the time variable  $t$  is capturing the temporal variation during the cardiac cycle.

### 2.2. Anatomical landmark model

A set of 33 anatomical landmarks, described in the next paragraph, are used to parameterize the complex and synchronized motion pattern of all valves, which explains the non-linearities of the hemodynamic movements. Thereby, each landmark is described by a  $T$  time-step trajectory in a three dimensional space, normalized by the temporal dependent similarity transform  $\mathbf{B}$ :

$$\mathbf{L}_n(\mathbf{B}) = \{l_1, l_2, \dots, l_T\} \quad n \in 1 \dots 33 \quad l_i \in \mathbb{R}^3 \quad (2)$$

### 2.3. Complete valve model

The final valves model is completed with a set of 13 dense surface meshes. Each mesh is sampled along anatomical grids of vertices defined through the landmarks:

$$\mathbf{V}_q(\mathbf{L}, \mathbf{B}) = \{\vec{v}_1, \vec{v}_2, \dots, \vec{v}_K\} \quad q \in 1 \dots 13 \quad \vec{v}_i \in \mathbb{R}^3 \quad (3)$$

where  $\vec{v}_i$  are the vertices, and  $K$  is the total number of vertices of mesh  $q$ . Each anatomical landmark, described in the previous section, has a fixed correspondence on the parameterized surface mesh.

#### 2.3.1. Aortic valve

Four surface structures represent the aortic valve: aortic root, left coronary leaflet, right coronary leaflet and non-coronary leaflet. The aortic root connects the ascending aorta to the left ventricle outflow tract and is represented through a tubular grid (see Fig. 2). This is aligned with the aortic circumferential  $u$  and ascending directions  $v$  and includes  $36 \times 20$  vertices and 1368 faces. The root is constrained by six anatomical landmarks, i.e. three commissures and three hinges, with a fixed correspondence on the grid. The three aortic leaflets, the L-, R- and N-leaflet, are modeled as paraboloids on a grid of  $11 \times 7$  vertices and 120 faces (see Fig. 6e). They are stitched to the root on a crown like attachment

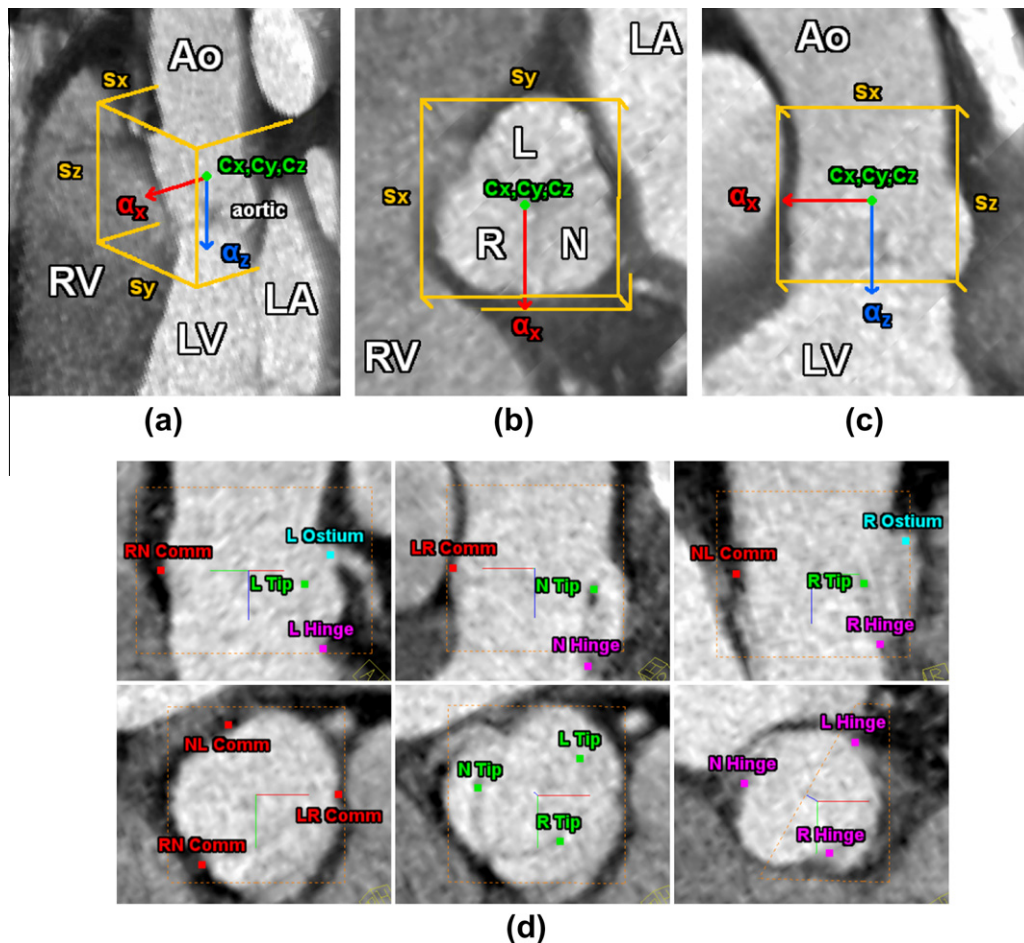


**Fig. 2.** Global motion and anatomical landmark model of the aortic valve. The similarity transform is represented as a bounding box around the aortic valve estimated from 4D cardiac CT. (a) Perspective view; (b) long axis; (c) short axis; (d) landmarks relative to the anatomical location illustrated in long and short axis from an example CT study.

ring, which defines the parametric  $u$  direction at the borders. The vertex correspondence between the root and leaflets along the merging curve is symmetric and kept fixed. The leaflets are constrained by the corresponding hinges, commissures and tip landmarks, where the  $v$  direction is the ascending vector from the hinge to the tip.

### 2.3.2. Mitral valve

The mitral valve is composed of 7 landmarks including 3 trigons, 2 commissures and 2 leaflet tips (see Fig. 3). The leaflets separate the left atrium and left ventricle hemodynamically and are connected to the endocardial wall by the saddle shaped mitral annulus. Both are modeled as paraboloids and their upper margins implicitly define the annulus. Their grids are aligned with the circumferential annulus direction  $u$  and the orthogonal direction  $v$  pointing from the annulus towards leaflet tips and commissures (see Figs. 6b and 6f). The anterior leaflet is constructed from  $18 \times 9$  vertices and 272 faces while the posterior leaflet is represented with  $24 \times 9$  vertices and 368 faces. Both leaflets are fixed by the mitral commissures and their corresponding leaflet tips. The left/right trigons and the postero-annular midpoint further confine the anterior and posterior leaflets, respectively.

### 2.3.3. Pulmonary valve

The representation of the pulmonary valve is compounded out of four structures: pulmonary trunk, left facing leaflet, none facing leaflet and right facing leaflet (see Fig. 4). The pulmonary trunk emerges out of the right ventricular outflow tract, supports the

pulmonary valves and its three leaflets, and ends at the level of the pulmonary artery bifurcation. The grid, which spans the pulmonary trunk surface, is aligned with the circumferential  $u$  and longitudinal direction  $v$  of the valve. It includes  $50 \times 40$  vertices and 3822 faces confined through the pulmonary commissures, hinges and the RV trigon. The attached L-, R- and N-leaflets, are modeled as paraboloids along the annulus circumferential direction  $u$  and vector  $v$  pointing from the corresponding hinge to the leaflet tip (see Fig. 6g). Each includes  $11 \times 7$  vertices and 120 faces bounded by the associated two commissures, hinge and tip.

### 2.3.4. Tricuspid valve

The function of the tricuspid valve is to regulate the blood flow from the right atrium to the right ventricle, staying closed during systole and opened during diastole. The model is constrained by four surface geometries (annulus, septal-, anterior- and posterior leaflet) (see Fig. 6h) and six anatomical landmarks (three commissures and three leaflet tips as illustrated in Fig. 5) which are corresponding to vertices on the meshes. The tricuspid annulus is represented as a surface mesh constrained by the three commissures. The tricuspid leaflets are modeled as hyperbolic paraboloids and implicitly describe the tricuspid annulus. Their grids are spanning along the annulus circumferential direction  $u$  and the perpendicular vector  $v$  pointing for the annulus towards the corresponding leaflet tip, and consist out of  $22 \times 14$  vertices and 546 faces. Each leaflet is constrained by the corresponding two commissures and one leaflet tip (see Fig. 6h).

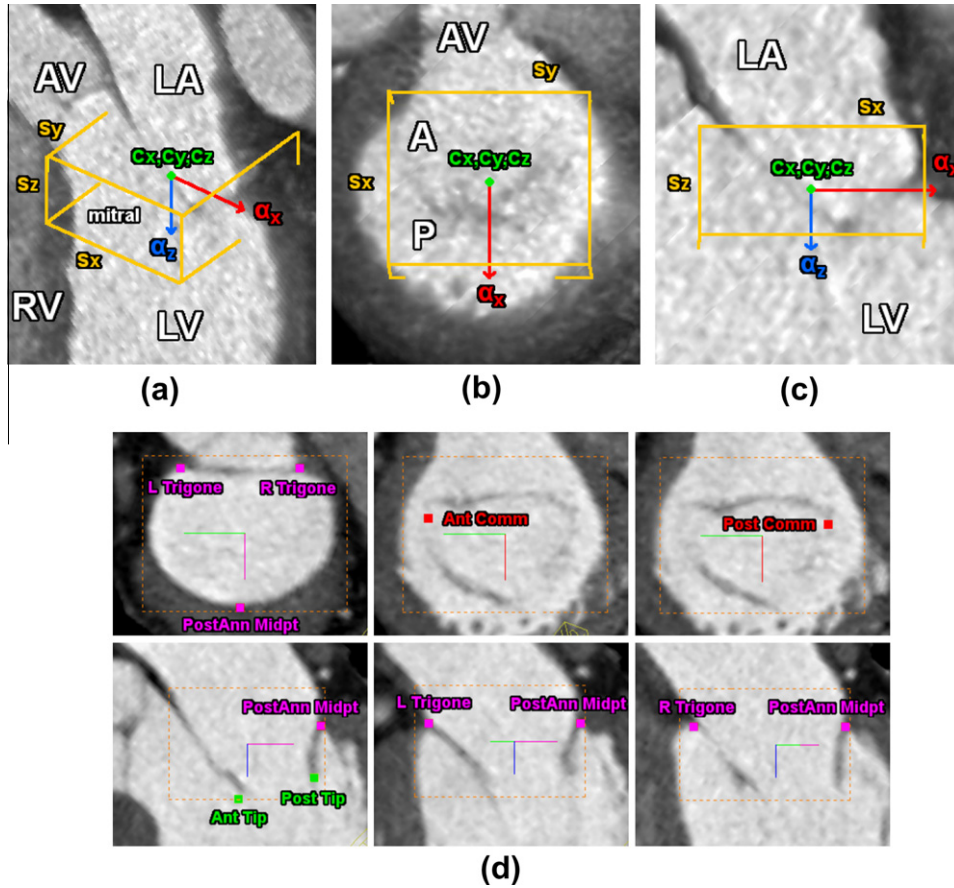


**Fig. 3.** Global motion and anatomical landmark model of the mitral valve. The similarity transform is represented as a bounding box around the mitral valve estimated from 4D cardiac CT. (a) Perspective view; (b) long axis; (c) short axis; (d) landmarks relative to the anatomical location illustrated in long and short axis from an example CT study.

### 3. Patient-specific model estimation

A hierarchical estimation approach is utilized to deduce model parameters, introduced in the previous section from 4D cardiac CT images. First, robust machine learning techniques are applied to estimate the global valves and anatomic landmarks parameters introduced in Eqs. 1 and 2. Second, we present the novel anatomical constrained Multi-linear Shape Model (cMSM), which effectively captures the complex spatio-temporal variation of all valves. Lastly, the cMSM is applied in a learning-based framework to estimate the complete valve model described in Eq. 3.

#### 3.1. Global motion estimation

The global motion estimation is formulated as a classification problem in order to estimate  $\mathbf{B}_t$  for each time step  $t$  independently from the corresponding volumes  $I(t)$ . The probability  $p(\mathbf{B}_t|I(t))$  can be modeled by a learned detector  $D$ , which evaluates and scores a large number of hypotheses for  $\mathbf{B}_t$ . To avoid an exhaustive search along a nine-dimensional space of  $\mathbf{B}_t$ , we apply the Marginal Space Learning framework (Zheng et al., 2008) and decompose the original parameter space into a subset of increasing marginal spaces:

$$\Sigma_1 \subset \Sigma_2 \subset \dots \subset \Sigma_n = \Sigma \quad (4)$$

The nine-dimensional space described by the similarity transform in a three-dimensional Euclidean space is decomposed as follows:

$$\begin{aligned} \Sigma_1 &= (c_x, c_y, c_z) \\ \Sigma_2 &= (c_x, c_y, c_z, \vec{\alpha}_x, \vec{\alpha}_y, \vec{\alpha}_z) \\ \Sigma_3 &= (c_x, c_y, c_z, \vec{\alpha}_x, \vec{\alpha}_y, \vec{\alpha}_z, s_x, s_y, s_z) \end{aligned} \quad (5)$$

where  $\Sigma_1$  represents the position marginal space,  $\Sigma_2$  the position + orientation marginal space and  $\Sigma_3$  the position + orientation + scale marginal space, which coincides with the original domain. Detectors are trained using the Probabilistic Boosting Tree using Haar and Steerable Features for each marginal space  $D_1$ ,  $D_2$  and  $D_3$ , and  $\mathbf{B}_t$  is estimated by gradually increasing the dimensionality. As described in Zheng et al. (2008), the 100 highest scored candidates are retained in  $\Sigma_1$ , 50 in  $\Sigma_2$  and 25 in  $\Sigma_3$ , such that the smallest subgroup which is likely to include the optimal solution is preserved.

To obtain a temporally consistent global location a RANSAC estimator is employed. To suppress temporally inconsistencies, we assume a constant model for the cardiac motion, which drives the global movement of the entire valvular apparatus. From randomly sampled candidates, the one yielding the maximum number of inliers is picked as the final motion. Inliers are considered within a distance of  $\sigma = 7$  mm from the current candidate and extracted at each time step  $t$ . The procedure is applied for each valve separately, in order to obtain the resulting time-coherent similarity transform  $\mathbf{B}_t$  assuming small displacements between consecutive frames.

#### 3.2. Landmark location and motion estimation

The landmarks parameters are estimated within the marginal space learning framework Zheng et al. (2008) using an algorithm

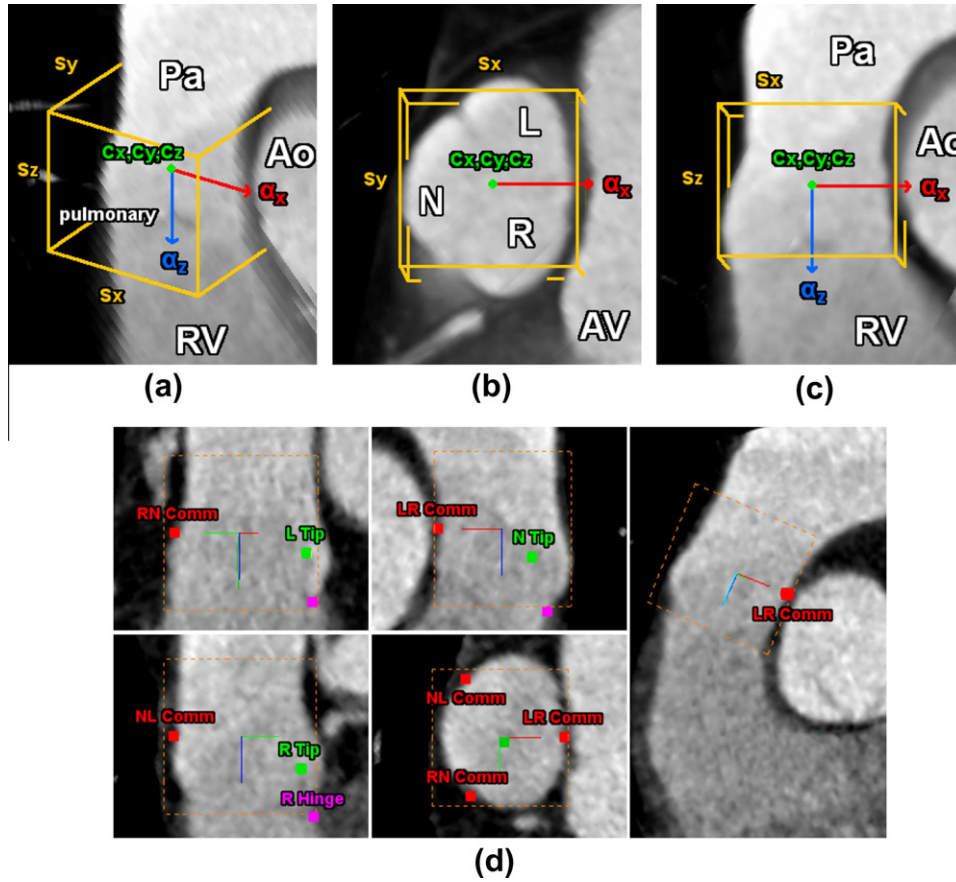


**Fig. 4.** Global motion and anatomical landmark model of the pulmonary valve. The similarity transform is represented as a bounding box around the pulmonary valve estimated from 4D cardiac CT. (a) Perspective view; (b) long axis; (c) short axis; (d) landmarks relative to the anatomical location illustrated in long and short axis from an example CT study.

called Trajectory Spectrum Learning (TSL), similar as in Ionasec et al. (2009). Hereby the landmark motions are represented in the frequency domain instead of the Euclidean space. Therefore the motion estimation problem is formulated as spectrum learning and detection in the trajectory space. The object localization and motion estimation, referred traditionally as detection and tracking are solved simultaneously.

The trajectory  $L_n(\mathbf{B})$  of each landmark can be uniquely represented by the concatenation of its discrete Fourier transform (DFT) coefficients,

$$\vec{s}^j = [\vec{s}^j(0), \vec{s}^j(1), \dots, \vec{s}^j(n-1)] \quad (6)$$

obtained through the DFT equation:

$$\vec{s}^j(f) = \sum_{t=0}^{n-1} L_n(\mathbf{B})(t) e^{-\frac{j2\pi f t}{n}} \quad (7)$$

where  $\vec{s}^j(f) \in \mathbb{C}^3$  is the frequency spectrum of the  $x$ ,  $y$ , and  $z$  components of the trajectory  $L_n(\mathbf{B})$ , and  $f=0, 1, \dots, n-1$ . A trajectory  $L_n(\mathbf{B})$  can be exactly reconstructed from the spectral coefficients  $\vec{s}^j$  applying the inverse DFT:

$$L_n(\mathbf{B}) = \sum_{f=0}^{n-1} \vec{s}^j(f) e^{\frac{j2\pi f t}{n}} \quad (8)$$

By decomposing the full trajectory space into orthogonal subspaces defined by generic bases, such as the Discrete Fourier Transform (DFT), the obtained representation is shown to be compact especially for periodic motions, such as the movements of the heart

valves. This resulting compact representation allows efficient learning and optimization in its marginal spaces. In the training stage, local features are extended in the temporal domain to integrate the time coherence constraint. Thereby simple gradient and intensity information is extracted from the image forming three-dimensional features  $F^{3D}()$ . As the motion of the landmarks is assumed to be locally coherent,  $F^{3D}()$  is applied in a temporal neighborhood  $t-T$  to  $t+T$ . The final value of the Local-Spatial-Temporal (LST) feature is the result of time integration using a set of linear kernels  $\tau$ , which weight the spatial features  $F^{3D}()$  according to their distance from the current frame  $t$ .

As described before the landmark trajectory is represented in the frequency space. Due to their periodic motion a small set of the frequency components is sufficient to represent their motion. These frequency subspaces  $\Sigma^{(k)}$  are efficiently represented by a set of corresponding hypotheses  $\mathcal{H}^{(k)}$  obtained from the training set. The pruned search space, restricted to  $\zeta$  frequency components, enables efficient learning and optimization:

$$\Sigma_{r-1} = \mathcal{H}^{(0)} \times \mathcal{H}^{(1)} \times \dots \times \mathcal{H}^{(r-1)}, \quad r = |\zeta| \quad (9)$$

The training algorithm starts by learning the posterior probability distribution in the marginal space  $\Sigma_0$ . Subsequently, the learned detectors  $D_0$  is applied to identify high probable candidates  $\mathcal{C}_0$  from the hypotheses  $\mathcal{H}^{(0)}$ . In the following step, the dimensionality of the space is increased by adding the next spectrum component. For each marginal space  $\Sigma_k$ , corresponding discriminative classifiers  $D_k$  are trained on sets of positives and negatives. The Local-Spatial-Temporal (LST) features are selected via the probabilistic boosting tree (PBT) to form the strong classifier  $D_k$ .

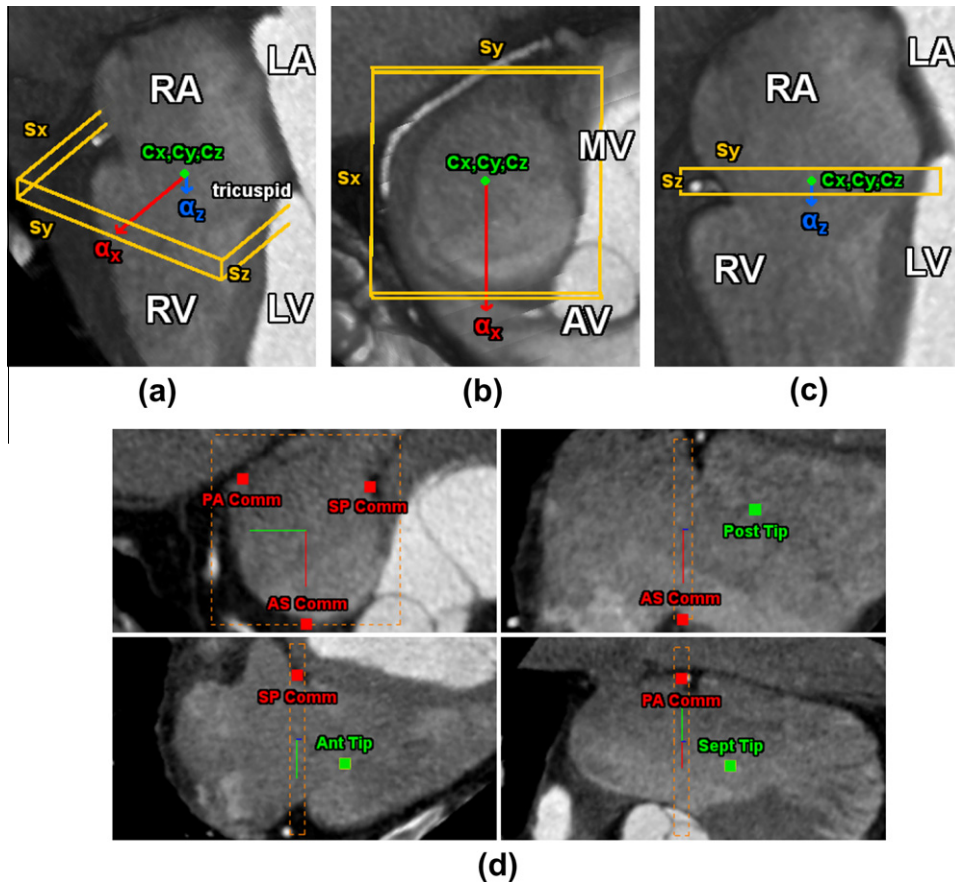


Fig. 5. Global motion and anatomical landmark model of the tricuspid valve. The similarity transform is represented as a bounding box around the tricuspid valve estimated from 4D cardiac CT. (a) Perspective view; (b) long axis; (c) short axis; (d) landmarks relative to the anatomical location illustrated in long and short axis from an example CT study.

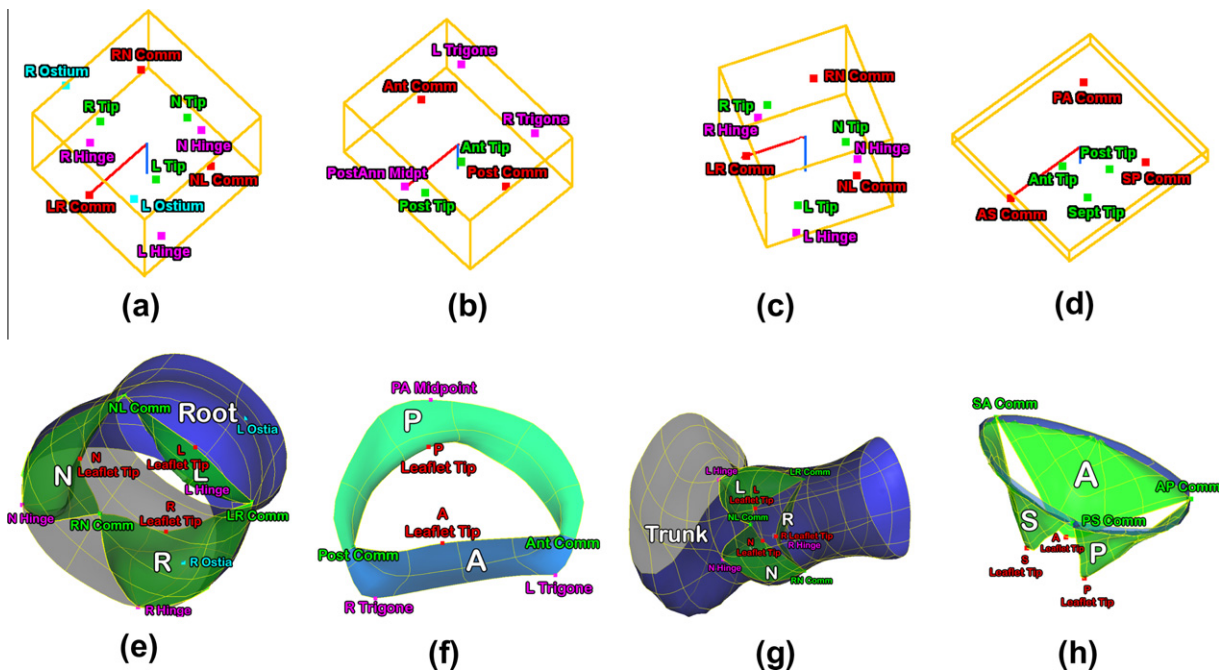


Fig. 6. Anatomical landmark model and complete valve model of the aortic valve, mitral valve, pulmonary valve and tricuspid valve.

In order to estimate the final trajectory of a landmark we start from the zero-spectrum and incrementally estimate the magnitude

and phase of each frequency component  $\vec{s}(k)$ . At the stage  $k$ , the corresponding robust classifier  $D_k$  is exhaustively scanned over

the potential candidates  $C_{k-1} \times \mathcal{H}^{(k)}$ . The final trajectory is reported as the average of all elements in  $C_{r-1}$ .

### 3.3. Constrained multi-linear shape model

Multilinear modeling enables the decomposition of a shape space in a temporal and spatial component in contrast to active shape models (ASM) where both are coupled. In this paper we present a Multi-linear MPCA (Multi-linear Principle Component Analysis) and MICA (Multi-linear Independent Component Analysis) shape model of all valves which is conditioned by anatomical measurements.

#### 3.3.1. Shape space

In order to construct the shape model all shapes  $\mathbf{V}$  are aligned by calculating the mean sequence model and aligning them using general procrustes analysis (GPA). This transform is utilized to align all shapes in the sequence. The normalized shapes are represented as third-order tensors  $\mathbf{D} \in \mathbb{R}^{(S \times T \times P)}$ , where  $S$  is the number of patients,  $T$  is the frame number inside a multi phase sequence and  $P$  represents the number of shape points.

$$\mathbf{D} = \mathcal{Z} \times_1 \mathbf{U}_{\text{patient}} \times_2 \mathbf{U}_{\text{motion}} \times_3 \mathbf{U}_{\text{points}} \quad (10)$$

where  $\mathbf{U}_{\text{patient}}$  is representing the patient modes,  $\mathbf{U}_{\text{motion}}$  the motion modes,  $\mathbf{U}_{\text{points}}$  the points modes and  $\mathcal{Z}$  the core tensor. As mentioned by Zhu et al. (2009) the motion subspace due its non-Gaussian distribution is decomposed using ICA and the patient and points space using PCA. We use the fixed point algorithm to perform the Independent Component Analysis (HyvSrinen et al., 2001). Thereby the Eq. 10 is modified by introducing the linear static transformation  $\mathbf{W}$ .

$$\begin{aligned} \mathbf{D} &= \mathcal{Z} \times_1 \mathbf{U}_{\text{patient}} \times_2 \mathbf{U}_{\text{motion}} \mathbf{W}^{-1} \mathbf{W} \times_3 \mathbf{U}_{\text{points}} \\ &= (\mathcal{Z} \times_2 \mathbf{W}) \times_1 \mathbf{U}_{\text{patient}} \times_2 \mathbf{U}_{\text{motion}} \mathbf{W}^{-1} \times_3 \mathbf{U}_{\text{points}} \\ &= \mathcal{S} \times_1 \mathbf{U}_{\text{patient}} \times_2 \mathbf{C}_{\text{motion}} \times_3 \mathbf{U}_{\text{points}} \end{aligned} \quad (11)$$

#### 3.3.2. Constrained model estimation

A crucial step in our hierarchical model estimation algorithm is to advance from one model hierarchy layer to the next finer. This step is especially important when moving from the anatomical landmark representation to the dense surface mesh models. Instead of using a warping technique, like the thin-plate spline interpolation, to map a mean mesh model to the location of the landmarks we use a Bayesian approach to estimate the dense surface meshes from meaningful clinical measures. A set of anatomical measurements  $\mathbf{M} (m_1, m_2, \dots, m_R)$  extracted from the non-linear

valve model is used to condition a surface parameterization  $\mathbf{V}_q$  ( $\vec{v}_1, \vec{v}_2, \dots, \vec{v}_K$ ) (Blanc et al., 2009). In the context of the aortic valve root  $\mathbf{V}_1$  three measurements are used: (1) inter-commissure distance, (2) hinge-leaflet tip distance and (3) inter-hinges distance (see Fig. 7).

Assuming the joint multivariate distribution  $(\mathbf{V}_q | \mathbf{M})$  follows a Gaussian distribution a conditioned surface  $\mathbf{V}_q^M$ , containing the anatomical measurements  $\mathbf{M}$ , can be estimated as follows:

$$\mathbf{V}_q^M = \mu_{\mathbf{V}_q} + \Sigma_{\mathbf{V}_q \mathbf{M}} \Sigma_{\mathbf{M} \mathbf{M}}^{-1} (\mathbf{M} - \mu_{\mathbf{M}}) \quad (12)$$

where  $\mu_{\mathbf{V}_q}$  is the mean surface parameterization from all training sets of the valve surface  $\mathbf{V}_q$ ,  $\mu_{\mathbf{M}}$  the mean of the measurements  $\mathbf{M}$  in the training set,  $\Sigma_{\mathbf{V}_q \mathbf{M}}$  the covariance matrix between  $\mathbf{V}_q$  and  $\mathbf{M}$ . The constrained surface  $\mathbf{V}_q^M$  is used to reconstruct the dynamic motion surface model of the whole sequence. Therefore we first estimate the patient modes  $\mathbf{u}_{\text{patient}}$  and then use them to reconstruct  $\mathbf{V}_q(\mathbf{L}, \mathbf{B})$ .

$$\mathbf{u}_{\text{patient}} = \mathbf{V}_q^M \mathbf{T}_{(1)}^{-1} \quad \mathcal{T} = \mathcal{S} \times_2 \mathbf{C}_{\text{motion}} \times_3 \mathbf{U}_{\text{points}} \quad (13)$$

where  $\mathbf{T}_{(1)}^{-1}$  is the pseudo-inverse of the tensor  $\mathcal{T}$  flattened along  $Z$   $Z \in 1 \dots T$  modes and  $\mathbf{C}_{\text{motion}}$  the  $Z$  dimensional motion modes. The complete surface model for the complete sequence, introduced in Eq. 3, can be extracted by a tensor multiplication:

$$\mathbf{V}_q(\mathbf{L}, \mathbf{B}) = \mathcal{S} \times_1 \mathbf{u}_{\text{patient}} \times_2 \mathbf{C}_{\text{motion}} \times_3 \mathbf{U}_{\text{points}} \quad (14)$$

### 3.4. Complete valve model estimation

The final stage in our hierarchical model estimation algorithm is the estimation of the complete surface model  $\mathbf{V}_q(\mathbf{L}, \mathbf{B})$ . The shape model of each valve is first initialized in the End-Diastole (ED) and End-Systole (ES) phases of the cardiac cycle using anatomical measurements  $\mathbf{M}$  defined between the landmarks  $\mathbf{L}_1 \dots \mathbf{L}_{33}$ . In the case of the aortic valve the shape is conditioned using three anatomical measurements extracted from the previously estimated landmark model:  $\mathbf{M} = \{m_1, m_2, m_3\}$  ( $m_1$ -inter-commissure distance,  $m_2$ -hinge-commissure plane distance,  $m_3$ -hinge-commissure plane angle). The initialized model is refined using a boundary detector  $D$  learned using the probabilistic boosting-tree (Tu, 2005) and steerable features (Freeman and Adelson, 1991). The detector  $D$  evaluates hypotheses for each discrete boundary point along its corresponding normal direction. The new boundary points are set to the hypotheses with maximal probability. To guarantee physiologically compliant results, the final model for each frame is obtained after projecting the estimated points to the multi-linear shape space described in Section 3.3. Thereby the multi-linear shape space is used as a parametric space limiting the variability

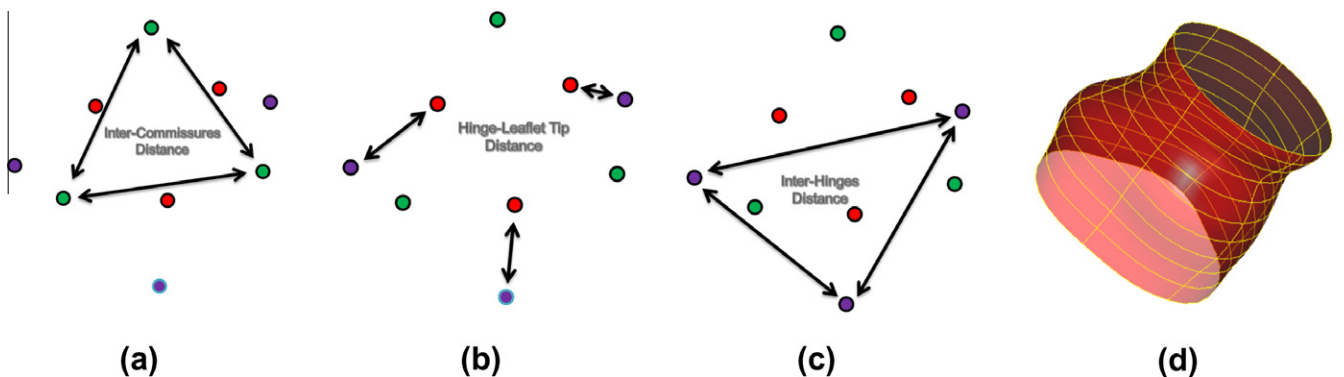


**Fig. 7.** Anatomical measurements extracted from the aortic valve anatomical landmarks model (a) inter-commissures distance, (b) hinge-leaflet tip distance and (c) inter-hinge distance in order to constrain the full surface model (d). The green points are representing the aortic valve commissures, the purple point the hinges and the red the leaflet tips.

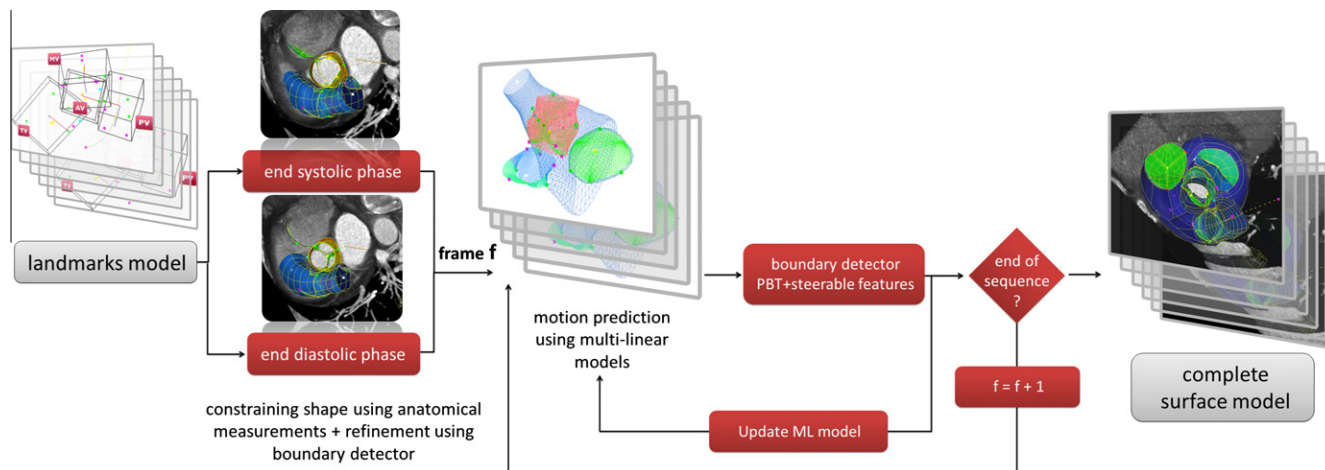


**Fig. 8.** Diagram depicting the estimation process of the complete valve model during a full cardiac cycle.

**Table 1**

Accuracy of the global location and rigid motion estimation, quantified from the box corners and reported using the mean error and standard deviation distribution over each valve.

	Aortic valve	Mitral valve	Pulmonary valve	Tricuspid valve
Mean error (mm)	4.32	6.72	7.72	8.12
STD (mm)	1.90	2.21	2.3	3.2

of the final shape model. Starting from the estimation results in the ED and ES phases, model parameters can be predicted in the remaining frames by utilizing the multi-linear shape model as described in Section 3.3. Thereby an initialization of the models is available in the remaining frames of the sequence and it is conditioned on the estimation results in the ED and ES frames. Starting from the neighboring frames  $t_{ED+1}$ ,  $t_{ED-1}$ ,  $t_{ES+1}$ ,  $t_{ES-1}$  the initialization is refined using the boundary detector  $D$  and the result projected to the parametric multi-linear shape space. Thereby the patient specific modes  $\mathbf{u}_{\text{patient}}$  are updated and thus the predictions in the remaining frames are more accurate as the variability or the dynamic shape model was reduced. The procedure is repeated until the full 4D model is estimated for the complete sequence (see Fig. 8).

#### 4. Experimental results

The accuracy of the proposed method was evaluated using cardiac CT data sets from patients affected by a large spectrum of cardiovascular and valvular heart diseases. Among the included pathologies are: regurgitation, stenosis, prolapse and aortic root dilation. The ECG gated cardiac CT sequences included multiple volumes per cardiac cycle, where each volume contains 80–350

slices with  $153 \times 153$ – $512 \times 512$  pixels. The in-slice resolution is isotropic and varies between 0.28 and 1.00 mm with a slice thickness from 0.4 to 2.0 mm. The imaging data set includes 64 cardiac CT studies (640 volumes) which were collected from several medical centers around the world. Using heterogeneous imaging protocols, cardiac CT exams were performed with Siemens Somatom Sensation or Definition scanners. Each sequence was acquired over one cardiac cycle and consisted of ten volumes. Only data sets which contained a contrast agent and all valves were visible were used. In order to keep the radiation dose low during the acquisition most of the data sets had one peak dose at either the ED or ES phase and a low dose during the rest of the cardiac cycle. Therefore the best visibility of the valves was during the peak dose phase and a moderate quality during the remaining cycle. The ground-truth for training and testing was obtained through an incremental annotation process. Therefore, each volume in our data set is associated with an annotation obtained through an expert-guided process that includes the following steps:

- The anatomical landmark motion model is manually determined by placing each anatomical landmark (see Section 2.2) at the correct location in the entire cardiac cycle of a given study. From the annotated anatomical landmark model, the global dynamic motion model  $\mathbf{B}_i$  is determined as described in Section 2.2.
- The complete valve model is initialized through its mean model placed at the correct image location, expressed by the thin-plate-spline transform estimated from the previously annotated anatomical landmark model (see Section 2.3).
- The annotation of the complete valve model is manually adjusted to delineate the true valves boundaries over the entire cardiac cycle (see Section 3.4). Complex resampling algorithms specialized for each valve were developed to ensure temporal and spatial consistency during the annotation process.

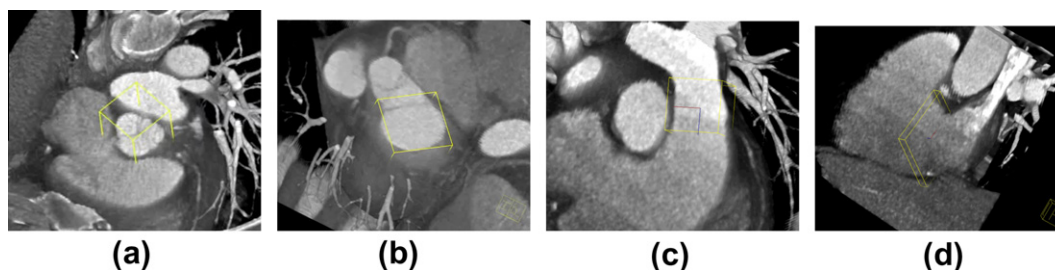


**Fig. 9.** Examples of global dynamic motion estimation in cardiac CT: (a) aortic valve, (b) mitral valve, (c) pulmonary valve, (d) tricuspid valve.

**Table 2**

Accuracy of the global location and rigid motion estimation reported separately for position, orientation and scale.

	Mean/STD	Median	80%
Position (mm)	3.09 ± 3.02	2.33	3.23
Orientation (deg)	9.72 ± 5.98	7.93	10.73
Scale (mm)	6.50 ± 4.19	5.09	7.81

**Table 3**

Accuracy of the non-rigid landmark motion estimation, quantified by the Euclidean distance and reported using the mean error and standard deviation distribution over each valve.

	Aortic valve	Mitral valve	Pulmonary valve	Tricuspid valve
Mean error (mm)	2.65	2.75	3.50	3.59
STD (mm)	1.50	1.19	2.53	2.55

In addition each evaluation is done using threefold cross-validation.

An inter-user experiment was conducted on a randomly selected subset of sixteen studies for the aortic and mitral valve. The patient-specific landmark valve models  $L_n(\mathbf{B})$  were manually fitted by four experienced users. The ground-truth was assumed to be the mean of the four user annotations. A landmark error of  $1.53 \pm 0.93$  mm for the aortic valve and  $1.97 \pm 1.4$  mm for the mitral valve was observed.

The performance of the global dynamic motion estimation,  $\mathbf{B}_t$ , described in Section 3.1, is evaluated in two distinct experiments. First, the overall detection precision is quantified at the box corners of the detected time-dependent similarity transformation. The average Euclidean distance between the eight bounding box points, defined by the similarity transform parameters  $\{(c_x, c_y, c_z)_i, (\vec{\alpha}_x, \vec{\alpha}_y, \vec{\alpha}_z)_i, (s_x, s_y, s_z)_i\}$  and the ground-truth box is reported. Table 1 illustrates the mean errors and corresponding standard deviations distributed over the four valves. Examples of estimation results are given in Fig. 9.

In a second experiment, the accuracy of the individual detection stages is investigated. Absolute differences between estimated and ground truth parameters of the position, orientation, and scale are reported in Table 2. The 80% column represents the 80th percentile of the error values. Please note that in order to speed up the algorithm, the estimation of the global location and rigid motion is always performed on downsampled data with an isotropic resolution of 3 mm.

The accuracy of the anatomical landmark motion model,  $L_n(\mathbf{B})$ , presented in Section 2.2 is measured using the Euclidean distance between detected and corresponding ground truth landmark trajectories. Table 3 demonstrates the precision expressed in mean errors and standard deviations, distributed over the four valves. Note that reported values are obtained by averaging the performance of

**Table 4**

Accuracy of the comprehensive valve model estimation, quantified by the point-to-mesh distance and reported using the mean error and standard deviation distribution over each valve.

	Aortic valve	Mitral valve	Pulmonary valve	Tricuspid valve
Mean error (mm)	1.22	1.32	1.35	1.40
STD (mm)	0.38	0.57	0.9	1.41

individual landmarks with respect to the corresponding valve. Examples of estimation results are given in Fig. 10. The detection was performed on volumes resampled to an isotropic resolution of 1 mm. Thus our automated landmark estimation error (1.53 mm for the aortic valve and 1.97 mm for the mitral valve) is slightly above (1.13 mm for the aortic valve and 0.78 mm for the mitral valve) the intra-user variability error (1.53 mm for the aortic valve and 1.97 mm for the mitral valve).

The accuracy of the algorithm in Section 2.3 to estimate the comprehensive valvular model,  $V_q(\mathbf{L}, \mathbf{B})$ , (see Section 3.4) is evaluated by utilizing the point-to-mesh distance. For each point on a surface  $V_q$ , we search for the closest point on the other surface to calculate the Euclidean distance. To guarantee a symmetric measurement, the point-to-mesh distance is calculated in two directions, from detected to ground truth surfaces and vice versa. Table 4 contains the mean error and standard deviation distributed over the four valves. The detection of the comprehensive valves model was performed on volumes resampled to an isotropic resolution of 1 mm. Examples of estimation results are given in Fig. 11.

In the second experiment we compared our new shape estimation approach with two other methods. Thereby the error is measured as the point-to-mesh distance between the estimated and ground-truth mesh. For all methods the estimation of the dynamic global motion  $\mathbf{B}_t$  and the anatomical landmark model  $L_n(\mathbf{B})$  is done as described in Section 2.2. The results, shown in Table 5 corroborate that our constrained ML PCA-ICA shape estimation approach achieves best performance, compared to a regular ML PCA-ICA method and a standard frame-wise estimation procedure (tracking by detection). Within three minutes a complete personalized dynamic model of all valves is estimated with an average accuracy of 1.24 mm. The full valvular model together with the four chambers of the heart is illustrated in Figs. 11 and 12.

Important clinical parameters are extracted from the personalized model in the right heart. They include right-ventricle outflow tract (RVOT) radius, bifurcation radius, tricuspid valve area and a joint measurement of the two valves, the pulmonary and tricuspid valve distance. Quantitative comparison is shown in Fig. 13 by comparing ground truth measurements and the estimated, demonstrating a strong correlation.

Finally we show quantitative comparison between a patient suffering from aortic valve regurgitation, a healthy patient and a post-operative patient who underwent a Ross operation. An impor-

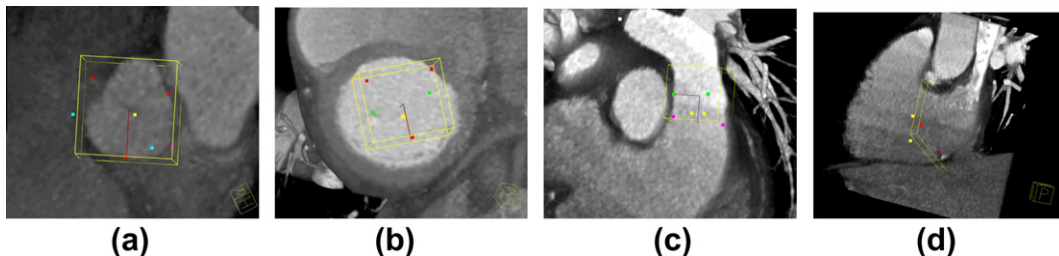


**Fig. 10.** Examples of the anatomical landmark motion estimation in cardiac CT: (a) aortic valve, (b) mitral valve, (c) pulmonary valve, (d) tricuspid valve. The colored points are showing the landmarks for each valve.

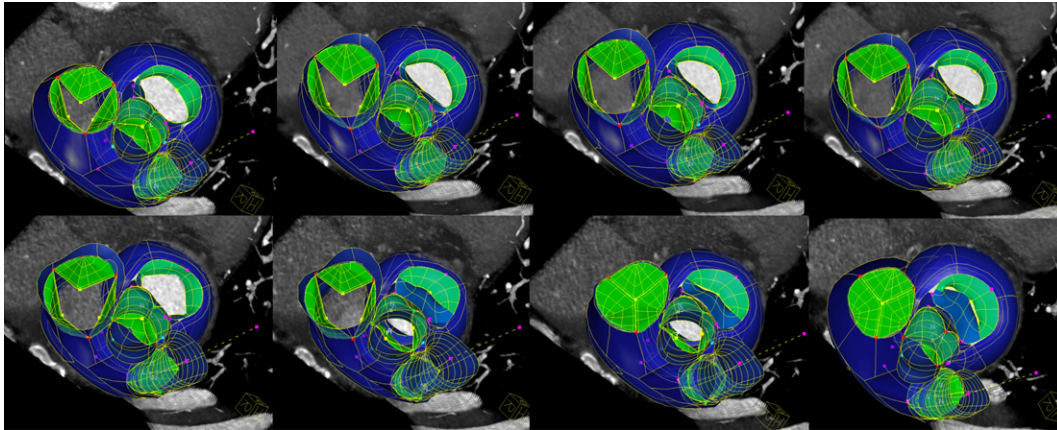


Fig. 11. Examples of the complete valves model estimation in cardiac CT of all heart valves during one cardiac sequence.

Table 5

System precision for valve model estimation averaged over all valves for comprehensive surface assessment.

	Mean	STD	Median
Tracking by detection (mm)	1.52	0.98	1.47
ML PCA-ICA (mm)	1.39	0.91	1.32
cML PCA-ICA (mm)	1.24	0.91	1.18

tant clinical measurement, the valvular area, extracted from the personalized aortic and pulmonary valve model, demonstrated in

Fig. 14, confirms a successful outcome since no regurgitation is observed at the aortic valve.

## 5. Discussion and conclusion

In this paper, we propose a novel personalized model for quantitative and qualitative evaluation of the complete heart valve apparatus in 4D CT. It is capable to delineate the full anatomy and dynamics needed to depict a large variation of valve pathologies, especially diseases affecting several valves. Its hierarchical

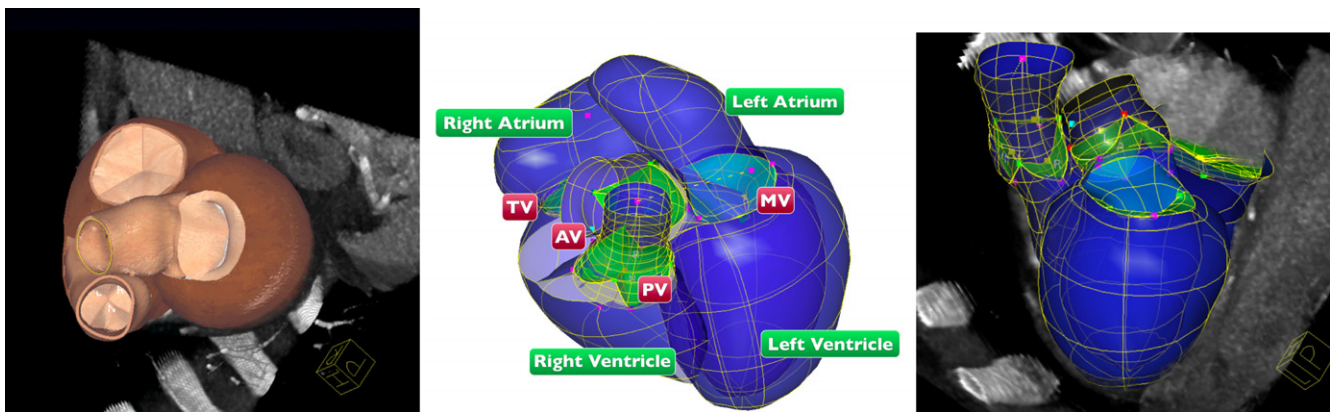


Fig. 12. Examples of estimated personalized model from a multiphase CT sequence. The images are extracted from the end-systolic phase.

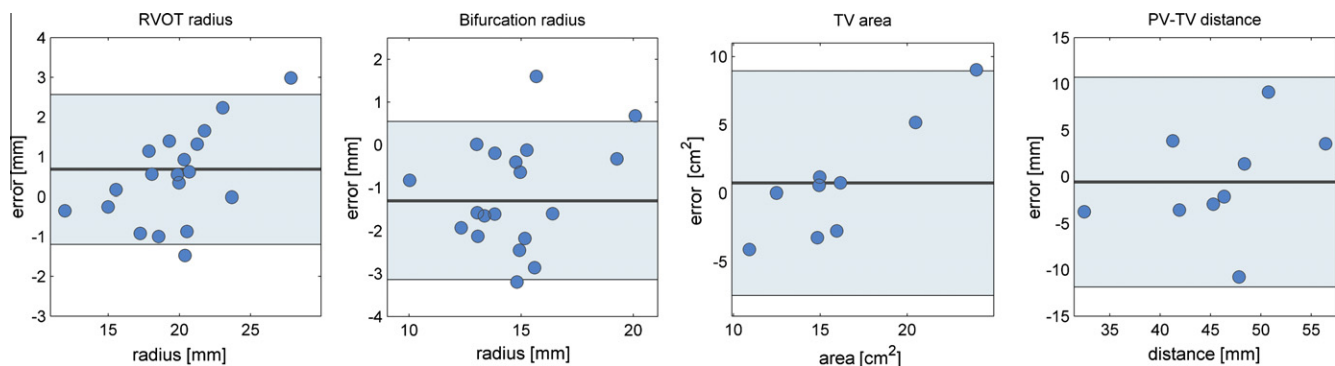
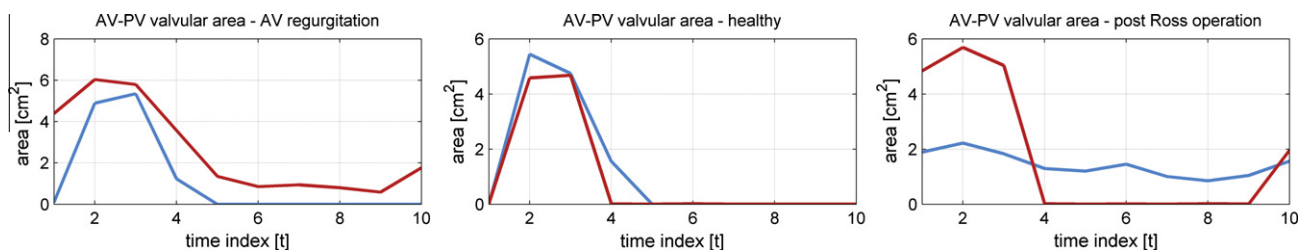


Fig. 13. Bland Altman plots for (a) right ventricle output tract diameter, (b) pulmonary valve bifurcation diameter, (c) tricuspid valve area and (d) distance between pulmonary and tricuspid valve. The ground truth measurements, derived from the models annotated by clinical experts, were compared with measurements derived from our automatically estimated models.



**Fig. 14.** Measurements of aortic (AV) and pulmonary valve (PV) area obtained from a patient with aortic valve regurgitation (left), a healthy patient (middle) and a post Ross operation patient (right). The red graph is representing the aortic valve and the blue the pulmonary. (For interpretation of the references to colour in this figure legend, the reader is referred to the web version of this article.)

approach using state of the art machine learning algorithms in combination with a constrained Multi-linear shape space enables patient specific model estimation within three minutes and an accuracy of 1.24 mm. Clinical validation shows strong correspondence between expert- and estimated anatomical measurements. Our approach enables for integrated quantification and treatment management of heart valves, and together with a patient specific chamber model (Zheng et al., 2007), it will enable comprehensive heart simulations. The proposed method could spark research in many areas such as examining interconnections of multiple valves and hemodynamic simulation of the complete cardiac apparatus.

Our experiments show that the automatic estimation of the valve models are slightly above (1.13 mm for the aortic valve and 0.78 mm for the mitral valve) the inter-user variability. Considering that our detection was done on 1 mm resolution this means that the deviation is around one additional voxel apart from the variability of the expert annotations. Data sets with low contrast agent, noise in the data and low imaging quality were the main reasons for the performance gap between the automatic estimation and the inter-user variability. As in most of our data sets the contrast agent was more concentrated in the left side of the heart and thus the estimation accuracy for the pulmonary and tricuspid valve was inferior to the aortic and mitral valve.

Future work will continue to focus the modeling side. One important extension will be the inclusion of the subvalvular apparatus of the mitral and tricuspid valves. Although critical in the clinical context, these structures are difficult to distinguish. Thus, patient-specific parameters must be inferred from statistical models or by fusing additional imaging information. The extension to a volumetric representation, which models the tissue thickness of the valves is also of high clinical importance. Such parameters could be estimated within the same discriminative learning framework, while the ground-truth for training and validation could come from in vivo measurements of resected tissue, post repair or replacement procedures.

## Appendix A. Supplementary material

Supplementary data associated with this article can be found, in the online version, at doi:10.1016/j.media.2012.02.003.

## References

- Blanc, R., Reyes, M., Seiler, C., SzTkely, G., 2009. Conditional variability of statistical shape models based on surrogate variables. In: Yang, G.Z., Hawkes, D., Rueckert, D., Noble, A., Taylor, C. (Eds.), *Medical Image Computing and Computer-Assisted Intervention, MICCAI 2009, Lecture Notes in Computer Science*, vol. 5762. Springer, Berlin/Heidelberg, pp. 84–91.
- Clapworthy, G., Viceconti, M., Coveney, P.V., Kohl, P., 2008. The virtual physiological human: building a framework for computational biomedicine. *Philosophical Transactions of the Royal Society A: Mathematical, Physical and Engineering Sciences* 366, 2975–2978.
- Conti, C., Stevanella, M., Maffessanti, F., Trunfio, S., Votta, E., Roghi, A., Parodi, O., Caiani, E., Redaelli, A., 2010. Mitral valve modelling in ischemic patients: finite element analysis from cardiac magnetic resonance imaging. In: *Computing in Cardiology*, 2010, pp. 1059–1062.
- Donald, L.J., Robert, A., Mercedes, C., Giovanni, D.S., Bruce, F.T., Katherine, F., Earl, F., Furie, K., Alan, G., Kurt, G., Nancy, H., Susan, H., Michael, H., Virginia, H., Brett, K., Steven, K., Daniel, L., Lynda, L., Ariane, M., Mary, M., James, M., Dariush, M., Graham, N., Christopher, O., Veronique, R., Wayne, R., Ralph, S., Paul, S., Randall, S., Julia, S., Thomas, T., Sylvia, W.S., Nathan, W., Judith, W.H., Yuling, H., 2009. Heart disease and stroke statistics – 2009 update: a report from the American Heart Association statistics committee and stroke statistics subcommittee. *Circulation* 119.
- Ecabert, O., Peters, J., Schramm, H., Lorenz, C., von Berg, J., Walker, M.J., Vembar, M., Olszewski, M.E., Subramanian, K., Lavi, G., Weese, J., 2008. Automatic model-based segmentation of the heart in CT images. *IEEE Transactions on Medical Imaging* 27, 1189–1201.
- Freeman, W., Adelson, E., 1991. The design and use of steerable filters. *IEEE Transactions on Pattern Analysis and Machine Intelligence* 13, 891–906.
- Fritz, D., Rinck, D., Dillmann, R., Scheuring, M., 2006. Segmentation of the left and right cardiac ventricle using a combined bi-temporal statistical model. In: *SPIE Medical Imaging*, pp. 605–614.
- Grbic, S., Ionasec, R., Vitanovski, D., Voigt, I., Wang, Y., Georgescu, B., Navab, N., Comaniciu, D., 2010. Complete valvular heart apparatus model from 4d cardiac ct. In: Jiang, T., Navab, N., Pluim, J., Viergever, M. (Eds.), *Medical Image Computing and Computer-Assisted Intervention, MICCAI 2010, Lecture Notes in Computer Science*, vol. 6361. Springer, Berlin/Heidelberg, pp. 218–226.
- Huang, J., Huang, X., Metaxas, D., Axel, L., 2007. Dynamic texture based heart localization and segmentation in 4-d cardiac images. In: *4th IEEE International Symposium on Biomedical Imaging: From Nano to Macro, 2007 (ISBI 2007)*, pp. 852–855.
- HyySrinen, A., Karhunen, J., Oja, E., 2001. *Independent Component Analysis*. John Wiley, Chichester.
- Ionasec, R., Voigt, I., Georgescu, B., Wang, Y., Houle, H., Vega-Higuera, F., Navab, N., Comaniciu, D., 2010. Patient-specific modeling and quantification of the aortic and mitral valves from 4-d cardiac ct and tee. *IEEE Transactions on Medical Imaging* 29, 1636–1651.
- Ionasec, R.I., Georgescu, B., Gassner, E., Vogt, S., Kutter, O., Scheuring, M., Navab, N., Comaniciu, D., 2008. Dynamic model-driven quantification and visual evaluation of the aortic valve from 4d ct. In: *MICCAI*, pp. 686–694.
- Ionasec, R.I., Voigt, I., Georgescu, B., Houle, H., Hornegger, J., Navab, N., Comaniciu, D., 2009. Personalized modeling and assessment of the aortic-mitral coupling from 4D TEE and CT. In: *MICCAI, Heidelberg*, pp. 767–775.
- Jablouk, A., 2007. National center for health statistics: National hospital discharge survey: annual summaries with detailed diagnosis and procedure data. *Data on Health Resources Utilization*, 13.
- Lansac, E., Lim, K.H., Shomura, Y., Goetz, W.A., Lim, H.S., Rice, N.T., Saber, H., Duran, C.M., 2002. Dynamic balance of the aortomitral junction. *The Journal of Thoracic and Cardiovascular Surgery* 123, 911–918.
- Lorenz, C., von Berg, J., 2006. A comprehensive shape model of the heart. *Medical Image Analysis* 10, 657–670, Special Issue on Functional Imaging and Modelling of the Heart (FIMH 2005).
- Mutlak, D., Aronson, D., Lessick, J., Reisner, S., Dabbah, S., Agmon, Y., 2009. Functional tricuspid regurgitation in patients with pulmonary hypertension. *CHEST*, 115–121.
- Schneider, R., Perrin, D., Vasilyev, N., Marx, G., del Nido, P., Howe, R., 2010. Mitral annulus segmentation from 3d ultrasound using graph cuts. *IEEE Transactions on Medical Imaging* 29, 1676–1687.
- Timek, T., Green, G., Tibayan, F., Lai, F., Rodriguez, F., Liang, D., Daughters, G., Ingels, N., Miller, D., 2003. Aorto-mitral annular dynamics. *Annals of Thoracic Surgery* 76, 1944–1950.
- Tu, Z., 2005. Probabilistic boosting-tree: learning discriminative models for classification, recognition, and clustering. In: *Tenth IEEE International Conference on Computer Vision, 2005 (ICCV 2005)*, vol. 2, pp. 1589–1596.
- Veronesi, F., Corsi, C., Sugeng, L., Mor-Avi, V., Caiani, E., Weinert, L., Lamberti, C., Lang, R., 2009. A study of functional anatomy of aortic-mitral valve coupling using 3D matrix transesophageal echocardiography. *Circulation: Cardiovascular Imaging* 2, 24–31.
- Waechter, I., Kneser, R., Korosoglou, G., Peters, J., Bakker, N., Boomen, R., Weese, J., 2010. Patient specific models for planning and guidance of minimally invasive aortic valve implantation. In: Jiang, T., Navab, N., Pluim, J., Viergever, M. (Eds.),

- Medical Image Computing and Computer-Assisted Intervention, MICCAI 2010, Lecture Notes in Computer Science, vol. 6361. Springer, Berlin/Heidelberg, pp. 526–533.
- Zheng, Y., Barbu, A., Georgescu, B., Scheuering, M., Comaniciu, D., 2007. Fast automatic heart chamber segmentation from 3d ct data using marginal space learning and steerable features. In: IEEE 11th International Conference on Computer Vision, 2007 (ICCV 2007), pp. 1–8.
- Zheng, Y., Barbu, A., Georgescu, B., Scheuering, M., Comaniciu, D., 2008. Four-chamber heart modeling and automatic segmentation for 3-d cardiac ct volumes using marginal space learning and steerable features. IEEE Transactions on Medical Imaging 27, 1668–1681.
- Zhu, Y., Papademetris, X., Sinusas, A., Duncan, J., 2009. A dynamical shape prior for lv segmentation from rt3d echocardiography. In: Yang, G.Z., Hawkes, D., Rueckert, D., Noble, A., Taylor, C. (Eds.), Medical Image Computing and Computer-Assisted Intervention, MICCAI 2009. Springer, Berlin/Heidelberg, pp. 206–213.
- Zhuang, X., Rhode, K., Razavi, R., Hawkes, D., Ourselin, S., 2010a. A registration-based propagation framework for automatic whole heart segmentation of cardiac mri. IEEE Transactions on Medical Imaging 29, 1612–1625.
- Zhuang, X., Yao, C., Ma, Y., Hawkes, D., Penney, G., Ourselin, S., 2010b. Registration-based propagation for whole heart segmentation from compounded 3d echocardiography, in: 2010 IEEE International Symposium on Biomedical Imaging: From Nano to Macro, pp. 1093–1096.